

# Over 240 Resonances on a Metasurface-Pixelated Silicon Wafer in an Octave-Spanning Terahertz Range

Jiaming Liu, Xu Fang,\* Wen Lyu, Xiaojiao Deng, and Xiaoping Zheng\*

Metasurfaces hold tremendous promise for various innovative sensing applications, thanks to their remarkable ability to manipulate light. A recent significant advancement in this research direction is using quasi-BIC (bound states in the continuum) metasurfaces for mid-infrared molecular sensing, which relies on creating a series of nearly uniformly spaced, sharp resonances on a single device. Although many studies have highlighted the potential of adopting this method in the terahertz (THz) regime, experimental demonstration is lacking. In this work, the first experimental demonstration of such frequency comb-like, quasi-BIC resonances on a single device is presented in the THz regime. By pixelating a 6-inch Si wafer with 25 different metasurfaces that possess both high-order quasi-BIC modes and a geometric scaling, a set of 241 sharp resonances ranging from 350 to 750 GHz is produced based on numerical simulation. By using a high-resolution vector network analyzer, 140 peaks that fall into the detection range from 500 to 750 GHz are confirmed experimentally, and their frequencies match well with the simulated results. By experimentally demonstrating frequency comb-like, quasi-BIC THz resonances on a single device, this work shows a new path for metasurface-based sensing in the THz regime.

sensing, but they often suffer from insufficient detection sensitivity and specificity. For example, the THz fingerprints of table sugar and some plastic explosives are very similar.<sup>[5]</sup> To distinguish such two substances reliably, a highly researched approach is to use a device (e.g., a spectral filter, or an analyzer that is in direct contact with the analytes) to create spectral features that are both sharp and frequency agile. This is a challenging task, but the emergence of metasurface research has cast new light on how to address it.

Metasurfaces are planar nano- or microstructures that enable a high level of control over electromagnetic waves,<sup>[6–12]</sup> and their potential for THz sensing is now widely acknowledged.<sup>[13,14]</sup> To address the aforementioned challenges in sensing, a potential metasurface-based solution is to use dynamic tuning to shift a single or a few resonances across a frequency range.<sup>[15–19]</sup> However, it is apparently very difficult to achieve both a high quality (high-Q) factor and a broad

frequency tuning range simultaneously. As opposed to this dynamic approach, we reveal in this work the possibility of a different, static approach, by demonstrating a set of over 240 static, high-Q, octave-spanning resonances on a single Si wafer.

Our device uses quasi-BIC (bound states in the continuum) modes in Si metasurfaces to create high-Q resonances. Photonic BIC modes are localized resonances that are completely decoupled from the continuous spectrum of the propagating field in the environment.<sup>[20,21]</sup> For BIC modes that are symmetry protected, breaking the symmetry can reduce them to quasi-BIC modes and produce sharp resonances in the output spectrum.<sup>[22–27]</sup> These quasi-BIC modes have been used to facilitate molecular barcoding in the mid-infrared, where a set of frequency comb-like resonance peaks are created by placing many metasurfaces on a single chip.<sup>[28]</sup> Such frequency comb-like resonances also have great application potential for THz sensing, as evident in a series of theoretical works published recently.<sup>[29–37]</sup> However, although many works have experimentally demonstrated quasi-BIC modes in the THz regime, they all show only a few resonance peaks.<sup>[38–41]</sup> In contrast, here we demonstrate in an experiment for the first time, quasi-BIC enabled, frequency comb-like resonances in the THz regime.


In the following discussion, we first describe the layout and the key features of our device that facilitate the frequency

## 1. Introduction

Terahertz (THz) research touches a plethora of application areas that range from 6G communications,<sup>[1]</sup> biomedicine,<sup>[2]</sup> and agriculture<sup>[3]</sup> to homeland security.<sup>[4]</sup> Many of these applications aim to utilize the THz spectrum for label-free and non-destructive

J. Liu, W. Lyu, X. Deng, X. Zheng  
Department of Automation  
Beijing National Research Center for Information Science and Technology  
Tsinghua University  
Beijing 100084, China  
E-mail: asean@mail.tsinghua.edu.cn

X. Fang  
School of Electronics and Computer Science  
University of Southampton  
Southampton SO17 1BJ, UK  
E-mail: x.fang@soton.ac.uk

 The ORCID identification number(s) for the author(s) of this article can be found under <https://doi.org/10.1002/adom.202301979>

© 2023 The Authors. Advanced Optical Materials published by Wiley-VCH GmbH. This is an open access article under the terms of the Creative Commons Attribution License, which permits use, distribution and reproduction in any medium, provided the original work is properly cited.

DOI: 10.1002/adom.202301979

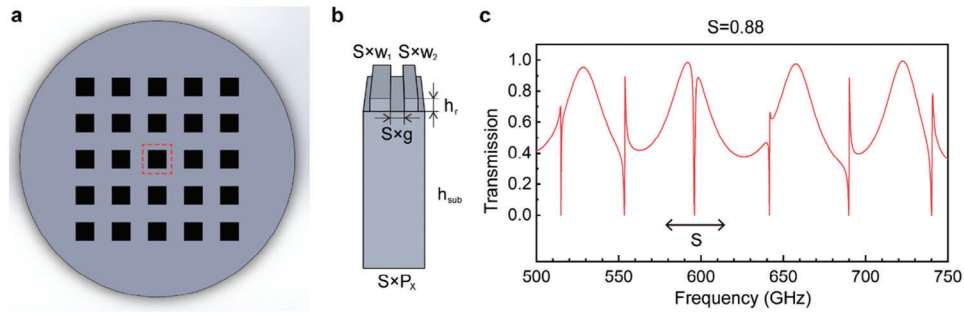


**Figure 1.** A Si wafer patterned with metagrating pixels. a) Schematic diagram of the pixelated Si wafer, showing an array of  $5 \times 5$  metagrating pixels. The red box highlights a single pixel. b) A meta-atom of a metagrating pixel. The meta-atom contains two parallel, cuboid-shaped ridges on top of a substrate. The two ridges are identical in height ( $h_r = 50 \mu\text{m}$ ) but differ in width ( $S \times w_1$  vs  $S \times w_2$ ), and they are separated along the  $x$  axis by a gap of  $S \times g$ . The substrate has a thickness of  $h_{\text{sub}}$  ( $625 \mu\text{m}$ ) along the  $z$  axis, and the meta-atom has a periodicity of  $S \times P_x$  along the  $x$  axis. The values of  $w_1$ ,  $w_2$ ,  $g$ , and  $P_x$  are fixed at  $79.2$ ,  $52.8$ ,  $54.0$ , and  $240.0 \mu\text{m}$ , respectively, throughout the wafer. The scaling factor  $S$  takes a unique value in each pixel, ranging from  $0.76$  to  $1.00$  at a step of  $0.01$ . c) A representative transmission spectrum, corresponding to a metasurface with a scaling factor  $S$  of  $0.88$ . The spectrum indicates these two key properties of the spectral resonances: multiple resonances exist in each metagrating, and their frequencies depend on the value of  $S$ . The metagrating is illuminated from the top at normal incidence, and the incident light is polarized along the ridges (i.e., along the  $y$  axis).

comb-like spectral output (Section 2.1). We then analyze the BIC modes in a hypothetical, mono-period metagrating (Section 2.2), before showing the transition from these BIC modes to quasi-BIC modes in the actual, dual-period metagratings (Section 2.3). We then show images of the sample and describe its fabrication and measurement (Section 2.4), before presenting all the simulated and the measured spectra together (Section 2.5).

## 2. Results and Discussion

### 2.1. Metagrating Pixels

In this work, we use a single 6-inch high-resistance Si wafer and pattern its surface with an array of  $5 \times 5$  different metasurfaces (Figure 1). Each metasurface pixel contains a dual period metagrating (Figure 1a), and a meta-atom (i.e., the unit cell) of these metagratings is depicted in Figure 1b. The meta-atom contains two cuboid-shaped ridges that are parallel along the  $y$  axis. In all the 25 metagratings, the thickness of the ridges and the substrate is  $50 \mu\text{m}$  (labeled as  $h_r$  in Figure 1b) and  $625 \mu\text{m}$  (as  $h_{\text{sub}}$ ), respectively. A critical feature of our design is the use of a scaling factor  $S$ . It controls these planar dimensions along the  $x$  axis: the periodicity of the meta-atom ( $S \times P_x$ ), the width of the two ridges ( $S \times w_1$  vs  $S \times w_2$ ), and the width of the inter-ridge gap ( $S \times g$ ). The values of  $w_1$ ,  $w_2$ ,  $g$ , and  $P_x$  are fixed at  $79.2$ ,  $52.8$ ,  $54.0$ , and  $240.0 \mu\text{m}$ , respectively, for all the metagrating. Meanwhile,  $S$  takes a different value for each metagrating, ranging from  $0.76$  to  $1.00$  at a step of  $0.01$ . As will be discussed in detail in the following sections, the wafer utilizes these two properties to maximize the number of resonance peaks for a given number of metagrating pixels: each metagrating supports multiple resonances, and these resonances shift in frequency with tuning  $S$  (Figure 1c).

### 2.2. High-Order BIC Modes

A key novelty of this work is its utilization of quasi-BIC resonances originating from high-order guided modes, the mechanism of which is discussed in detail in these two sections. This

section explores the origin and the characteristics of a series of high-order BIC modes, which lays the groundwork for the analysis of the high-order quasi-BIC modes in the following section. To reveal the design principle, we first pick the metagrating with  $S = 1.00$ , apply small modifications to its geometry, and analyze its electromagnetic properties in detail (Figure 2). To start with the analysis, we change the ridge widths  $S \times w_1$  ( $79.2 \mu\text{m}$ ) and  $S \times w_2$  ( $52.8 \mu\text{m}$ ) to their average value of  $66 \mu\text{m}$ . This modification converts the dual-period grating to a simpler, mono-period grating, which has a unit cell size of  $P = 120 \mu\text{m}$ . This new grating supports a series of diffraction orders under normal incidence, which can be expressed as:

$$k_{x,m} = k_0 + m \cdot 2\pi/P \quad (1)$$

Here,  $k_{x,m}$  is the  $x$  component of the wave vector of the  $m$ -th order diffraction, and  $k_0$  is the wave vector of the incident light. Figure 2a shows the dispersion of the first two diffraction orders,  $k_{x,1}$  and  $k_{x,2}$ , derived analytically from Equation (1).

Meanwhile, if we remove the ridges and consider only the flat substrate that has a thickness of  $h_{\text{sub}}$ , we can calculate its eigenmodes analytically.<sup>[42]</sup> As the incident light is  $\gamma$  polarized, only the TE modes need to be considered here, which can be expressed as:

$$\tan \left( h_{\text{sub}} \sqrt{k_0^2 n_{\text{sub}}^2 - \beta^2} \right) = \frac{2 \sqrt{(k_0^2 n_{\text{sub}}^2 - \beta^2) (\beta^2 - k_0^2)}}{(k_0^2 n_{\text{sub}}^2 - \beta^2) - (\beta^2 - k_0^2)} \quad (2)$$

Here,  $n_{\text{sub}} = 3.4176$  is the refractive index of Si,<sup>[43]</sup> and  $\beta$  is the propagation constant of a TE mode. Equation (2) serves as a guidance for us to find the resonances in our device, as adding a grating on top of the substrate disturbs the resonances, rendering this equation as an analytical approximation.

Figure 2a shows the TE eigenmodes of the hypothetical, mono-period grating, identified numerically by using a commercial finite element solver (COMSOL Multiphysics). In the simulation, the ridges were assumed to be infinitely long and the metagrating was assumed to be infinitely large. Figure 2a shows that each

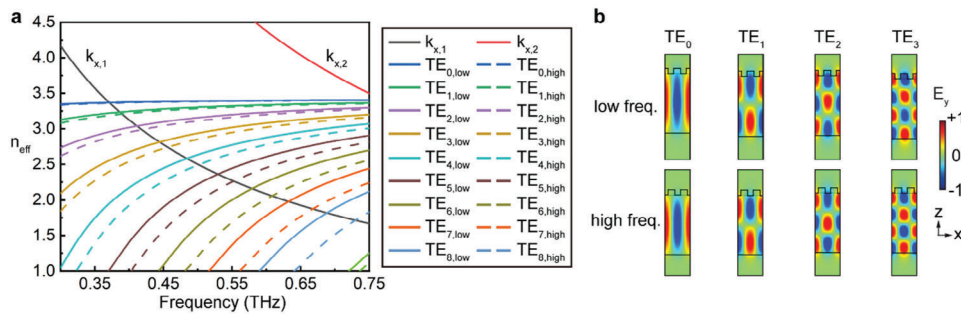


**Figure 2.** Properties of high-order BIC modes in a mono-period grating. a) The dispersion curves of diffraction wave vector  $k_{x,m}$  and TE eigenmode propagation constant  $\beta$  for a hypothetical, mono-period grating. The  $k_{x,m}$  curves are analytically calculated based on Equation (1), while the  $\beta$  curves are numerically calculated by using eigenmode analysis. The mono-period grating has a ridge periodicity of 120  $\mu\text{m}$ , created by setting a uniform ridge width of 66  $\mu\text{m}$ . The gap between two adjacent ridges, which now belong to two different unit cells, is 54  $\mu\text{m}$ . The first nine TE modes (from  $TE_0$  to  $TE_8$ ) are plotted in nine different colors. Each mode has two branches, with the low-frequency one and the high-frequency one drawn in a solid line and a dashed line, respectively. b) The  $y$  component of the electric field ( $E_y$ ) for both branches of the first four TE modes. They correspond to the first eight points that the  $k_{x,1}$  line intersects the TE lines. Each map covers two-unit cells.

TE mode is split into two branches, and the deviation between these two branches increases with the order of the mode. We refer to these two branches as the low-frequency branch and the high-frequency branch, as they have different frequencies at the same effective index  $n_{\text{eff}} (= k_0/\beta)$ . This difference in frequency is associated with a difference in the field distribution in space. Figure 2b shows the first four TE modes ( $TE_0$ – $TE_3$ ) as examples. The order number is associated with the number of the maximum field strength (i.e., locations where the normalized electric field takes either +1 or –1) along the vertical  $z$  axis. The number of these maxima increases from one for  $TE_0$  to four for  $TE_3$ . For each mode order, the two branches have an almost identical field pattern, but bear a horizontal offset. For the low-frequency branch, the maximum field strength inside the substrate aligns with the ridges. Meanwhile, the high-frequency branch is located between two adjacent ridges.

Figure 2a shows that the dispersion curves of the diffraction  $k_{x,1}$  and the guided TE modes  $\beta$  intersect at many points. However, this does not imply that the eigenmodes shown in Figure 2b can be excited by the incident light. In fact, for an infinitely large grating under the illumination of a plane wave at normal incidence, all of the intersection points in Figure 2a are protected by the symmetry of the system. They cannot be excited by the  $y$ -polarized, normal incident light, and they do not produce any spectral feature in the far field.

### 2.3. High-Order Quasi-BIC Modes

In order to utilize these guided TE modes for THz sensing, the geometric symmetry of the mono-period grating has to be slightly broken to convert the BIC modes to quasi-BIC modes. Figure 3 shows this conversion, by introducing a contrast between the ridge widths  $w_1$  and  $w_2$ . This geometric contrast converts the mono-period grating into a dual-period grating. A parameter  $\alpha_w$  called the degree of asymmetry, is used here, which is expressed as the normalized difference between  $w_1$  and  $w_2$  as:

$$\alpha_w = |w_1 - w_2| / |w_1 + w_2| \quad (3)$$

As an example to reveal the influence of  $\alpha_w$  on the metagrating spectrum, we pick the  $TE_2$  mode shown in Figure 2 and analyze its properties in Figure 3.

Figure 3a shows the numerically simulated transmission map for a series of metagratings, produced by adjusting  $\alpha_w$  from 0 to 0.9. It is worth highlighting that, all of the metagratings are still based on the dual period metagrating with  $S = 1.00$ . They all have a meta-atom periodicity  $S \times P_x = 240 \mu\text{m}$ . The value of  $w_1 + w_2$  and the center-to-center distance between the two ridges are also independent of  $\alpha_w$ , with both remaining at 120  $\mu\text{m}$ . At  $\alpha_w = 0$ , which corresponds to the BIC mode discussed in Figure 2, the transmission (the bottom line of the map) shows a gradual change with frequency across the whole frequency range, and there is no sharp resonance. Once  $\alpha_w$  increases above zero, a sharp resonance at 0.407 THz emerges. This radial transition reveals the creation of a quasi-BIC mode that is detectable in the far field. As  $\alpha_w$  further increases, the resonance gradually broadens and increases in frequency, with the transmission dip reaching 0.410 THz at  $\alpha_w = 0.9$ .

To better visualize this spectral dependence on  $\alpha_w$ , the transmission spectra of four representative values of  $\alpha_w$  (0, 0.2, 0.5, and 0.8) are plotted in Figure 3b. The spectrum of  $\alpha_w = 0$  is associated with a BIC mode, but this mode is undetectable. The other three spectra are each associated with a quasi-BIC mode, which appears as a resonance peak. For these quasi-BIC modes, the Q-factor decreases with increasing  $\alpha_w$ . These quasi-BIC modes also change in their electromagnetic near-field. Figure 3c compares the three quasi-BIC modes at their resonance frequencies (i.e., the transmission dip of the top three spectra in Figure 3b). As the resonance becomes broader in Figure 3b, the strength of the near field becomes weaker in Figure 3c.

Figure 3d quantifies the influence of  $\alpha_w$  on the quasi-BIC modes by using the Q-factor and the field enhancement factor  $|E_{\text{max}}/E_0|$ . These two factors complement each other in the analysis, with the former related to the far-field (i.e., the transmission spectrum) and the latter to the near-field (i.e., the strongest field strength in the near-field normalized against the incident field). The Q-factor is extracted from each spectrum embedded in Figure 3a, by fitting the transmission  $T$  using the Fano resonance equation.<sup>[44,45]</sup> The equation is expressed as

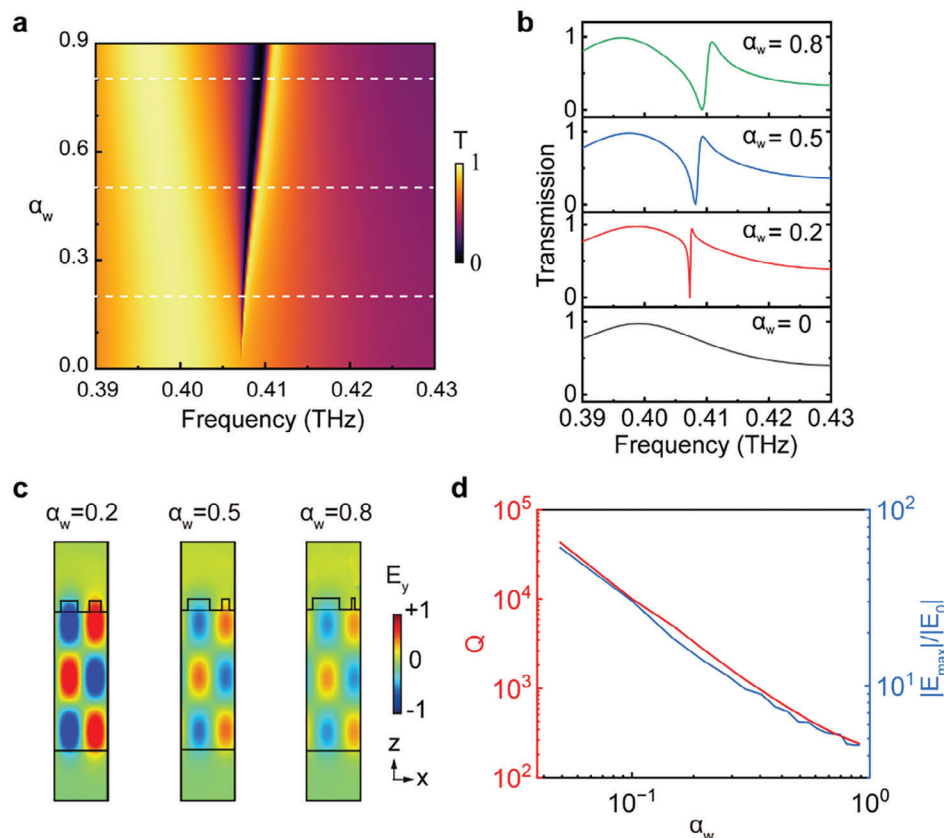


**Figure 3.** Reducing the BIC modes to quasi-BIC modes by adjusting the degree of asymmetry  $\alpha_w$ . a) Transmission map showing the transition from the BIC mode to the quasi-BIC mode, as well as the evolution of the quasi-BIC mode with  $\alpha_w$ . b) Four representative transmission spectra were extracted from the map, with  $\alpha_w$  at 0, 0.2, 0.5, and 0.8. They correspond to the bottom line and the three white dashed lines in the map. c) Field distribution at the resonance frequency of the three representative quasi-BIC modes (i.e., those with  $\alpha_w$  at 0.2, 0.5, and 0.8). The field is normalized against the maximal value of the three maps. Each map shows a single meta-atom. d) The influence of  $\alpha_w$  on the Q-factor and the field enhancement factor  $|E_{max}/E_0|$ .

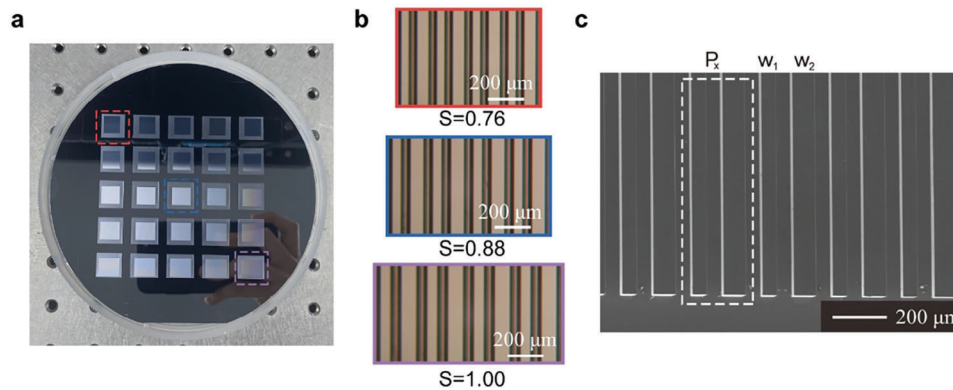
$T = |a_1 + i a_2 + b/(f - f_0 + i \gamma)|^2$ , where  $a_1 + i a_2$  is the resonance-free background, and  $b, f_0$ , and  $\gamma$  are the amplitude, the peak frequency and the dissipation rate of the resonance. The fitting then allows for the Q-factor to be determined by using  $Q = f_0/(2 \gamma)$ .

Figure 3d shows the values of the Q-factor and the  $|E_{max}/E_0|$  factor, with  $\alpha_w$  ranging from 0.05 to 0.90. The lower limit of  $\alpha_w$  is set at 0.05, as the computing power required for the calculation increases steeply as  $\alpha_w$  approaches zero. At  $\alpha_w = 0.05$ , the Q-factor and the  $|E_{max}/E_0|$  factor reach the highest values of  $4.3 \times 10^4$  and 60.8, respectively. As  $\alpha_w$  increases, both factors decrease sharply. The Q-factor is inversely proportional to the square of the asymmetric factor  $\alpha_w$  (i.e.,  $\propto \alpha_w^{-2}$ ), which is consistent with previous works on quasi-BIC resonances.<sup>[46]</sup> The  $|E_{max}/E_0|$  factor also decreases with increasing the asymmetric factor  $\alpha_w$  but at a slower rate (roughly proportional to  $\alpha_w^{-1}$ ). The  $|E_{max}/E_0|$  factor appears to be more susceptible to numerical fluctuation as compared to  $\alpha_w$ . This is attributed to the fact that each data point on the  $|E_{max}/E_0|$  line is extracted from the calculation at a single frequency (as in Figure 3c), whilst each data point on the  $\alpha_w$  line is derived from the calculation of a range of frequencies (as in Figure 2b).

It is worth pointing out that, although reducing the level of symmetry is widely accepted as a necessary condition for reducing a symmetry-protected BIC mode to a quasi-BIC mode,<sup>[20,21]</sup>

it is not a sufficient condition. As Figure 3 shows, the high-frequency branch of the  $TE_2$  mode remains hidden, even when the degree of asymmetry  $\alpha_w$  is non-zero. In fact, in our measured sample, only the low-frequency TE branches are visible in the spectra, while all the high-frequency TE branches remain as symmetry-protected BIC modes. This contrast originates from their different  $C_2$  symmetry (i.e., twofold rotational symmetry). As Figure 3c shows, the low-frequency modes have odd  $C_2$  symmetry. Their near-field distribution follows the geometry of the metagrating, with the field beneath the two ridges equal in amplitude and opposite in sign. This symmetry matches with that of the incident light and makes these modes visible. Meanwhile, the high-frequency modes have the opposite (i.e., even)  $C_2$  symmetry, so they remain hidden in the spectrum even when  $\alpha_w$  is non-zero. These hidden high-frequency modes can appear in the spectrum, by further removing the symmetry protection in the dual-period grating (e.g., by adjusting the horizontal positions of the two ridges).

The results of Figure 3 provide useful guidance for our experiment. They show that, in order to make spectral peaks sharp and narrow, a small  $\alpha_w$  should be chosen. On the other hand, if a peak is too sharp, it will pose challenges to experimental verification: 1) the peak characteristics will become very sensitive to a small fluctuation in  $\alpha_w$ , which cannot be eliminated in microfabrication; 2)



**Figure 4.** Images of the Si wafer that contains 25 metagrating pixels. a) Image of the whole wafer taken using a smartphone. Each of the 25 pixels has a unique value of the scaling factor  $S$ , which changes from 0.76 in the top left pixel to 1.00 in the bottom right pixel. These two corner pixels, together with the pixel at the center ( $S = 0.88$ ), are highlighted using colored boxes. b) Optical microscope images of these three metagratings. Only a section of four meta-atoms is shown for each metagrating. The white bar represents a length of  $200\ \mu\text{m}$  for all images. c) An SEM image for the pixel with  $S = 0.88$ . A meta-atom is highlighted, and the parameters  $P_x$ ,  $w_1$ , and  $w_2$  are marked out in the image.

the peak can be easily missed in a frequency scan if the measurement facility does not provide an extremely high-frequency resolution. Considering these facts, we choose  $\alpha_w = 0.20$  for all the 25 metagrating pixels in our experiment. With a universal value of  $\alpha_w$  adopted, the geometric differences of these 25 pixels are consequently attributed to a single parameter  $S$ . Tuning the value of  $S$  shifts the intersection points between the curves of  $k_{x,1}$  and  $\beta$  for the quasi-BIC modes, which can be derived following the analysis of Figure 2. It consequently shifts the resonance frequency of each quasi-BIC mode, which will be analyzed in Section 2.5.

#### 2.4. Si Wafer Pixelated with Metagratings

Based on the aforementioned analysis, we fabricated a set of 25 metagratings on a high-resistance Si wafer (Figure 4). The wafer has a diameter of 6 inches and a thickness of  $675\ \mu\text{m}$ . Following the numerical simulation, patterns are etched to a depth of  $50\ \mu\text{m}$ , leaving a substrate thickness of  $625\ \mu\text{m}$ . As regard to the planar dimensions and the spacing of the metagratings, they are determined by a few factors. They include: the wafer diameter (6 inches); the beam diameter of our THz measurement system ( $\approx 5\ \text{mm}$ ); and our initial target number of spectral peaks in an octave of THz frequency band ( $>100$ , by referencing to recent theoretical works listed in Table 1). By balancing these factors, we choose to have an array of  $5 \times 5$  metagrating pixels, a planar size of  $10\ \text{mm} \times 10\ \text{mm}$  for each pixel, and a spacing of  $10\ \text{mm}$

between adjacent metagratings in both directions (Figure 4a). As stated in Section 2.1, the values of  $w_1$ ,  $w_2$ ,  $g$ , and  $P_x$  are universal ( $79.2$ ,  $52.8$ ,  $54.0$ , and  $240.0\ \mu\text{m}$ , respectively) across the whole wafer, while the value of  $S$  changes from 0.76 (the top left pixel) at a step of  $0.01$ – $1.00$  (the bottom right pixel). Figure 4b,c is optical microscope images and a scanning electron microscope (SEM) image of the sample, respectively, and they show a high level of microfabrication accuracy. Details of the microfabrication process can be found in Experimental Section.

A vector network analyzer (VNA) was used to measure the transmission of each pixel. The VNA had a superior frequency resolution of  $0.1\ \text{GHz}$  that was ideal to resolve the sharp quasi-BIC peaks, but its frequency range was limited to  $500$ – $750\ \text{GHz}$ . The Si wafer was illuminated from the patterned side at normal incidence, and the normal incidence was guaranteed by using a high-precision rotation stage and a visible laser. The incident THz beam was raster scanned throughout all the pixels, and a whole set of 25 spectra was collected at the end. Components of the measurement system are described in detail in Experimental Section.

#### 2.5. Quasi-BIC Peaks of the Wafer

To demonstrate excellent matching between simulation and measurement, Figure 5 compares the experimental results of five representative metagratings ( $S$  from 0.96 to 1.00) against their

**Table 1.** Comparison with state-of-the-art, microstructure-based multiplexing technologies in the THz regime. For the number of digits after the decimal point in the frequency column, it follows the original values for the four references, and it is set as three for our own work.

Microstructure	Frequency [THz]	Resonance Number	Peak Density [ $\text{GHz}^{-1}$ ]	Measured /Simulated
Metal bars in mesh <sup>[32]</sup>	0.46–0.60	25	0.18	Simulated
Cylinder dimers metasurface <sup>[37]</sup>	0.47–0.59	70	0.58	Simulated
Inverted metagratings <sup>[35]</sup>	0.49–0.58	44	0.49	Simulated
Resonators with graphene micro-ribbons <sup>[33]</sup>	1.2–2.7	75	0.05	Simulated
Dual-period dielectric metagratings (this work)	0.500–0.750	140	0.56	Measured
	0.350–0.750	241	0.60	Simulated

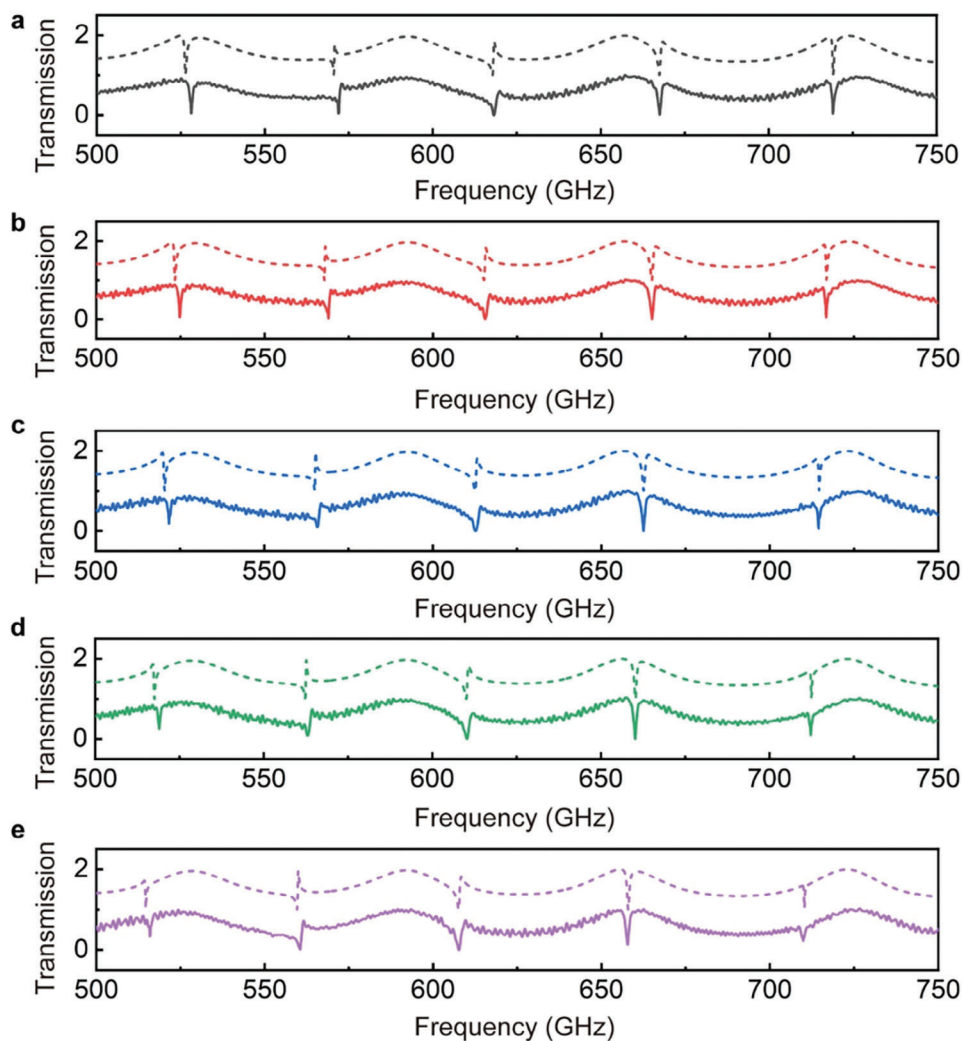


**Figure 5.** Simulated (dotted lines) and experimental (solid lines) transmission spectra of five representative metagratings. The  $S$  value is a) 0.96, b) 0.97, c) 0.98, d) 0.99, and e) 1.00. The frequency range shown here (from 500 to 750 GHz) is set by our measurement system. All the spectra, including both the experimental and the simulated ones, are sampled at a frequency interval of 0.1 GHz. All the simulated spectra have been shifted upward by 1.0 for visualization.

corresponding simulated results. Five resonance peaks are observed in each spectrum between 500 and 750 GHz. Near-field analysis shows that they correspond to the guided  $TE_5$ - $TE_9$  modes, with  $TE_5$  and  $TE_9$  at the low-frequency end and the high-frequency end, respectively. An excellent matching between the experimental and the simulated results is clearly observed. To quantify the matching, we calculate the relative frequency difference  $(f_m - f_s)/f_s$  for each peak, where  $f_m$  and  $f_s$  are the measured and the simulated peak frequencies, respectively. For all the 25 peaks, the maximal value of  $(f_m - f_s)/f_s$  is 0.32%, and the average of the absolute difference  $|f_m - f_s|/f_s$  is 0.11%. Both values are very small, and they are attributed to experimental imperfections, such as small deviations from the design values in geometric parameters. The values of  $f_m$ ,  $f_s$  and  $(f_m - f_s)/f_s$  for these five pixels can be found in Table S1 (Supporting Information), where all the simulated and measured quasi-BIC peaks are listed.

By scanning through all the 25 metagrating pixels, we identify a total of 140 resonance peaks in the experimental frequency range from 500 to 750 GHz (Figure 6). In order to reveal different aspects of this result, Figure 6a,b plots the 25 spectra in two different ways. In Figure 6a, the 25 spectra are overlaid on top of each other, but only the peaks are plotted for visualization (i.e., the 25 spectra have been sliced into sections and then stitched together). At the low-frequency end (i.e., close to 500 GHz), the sensitivity of our VNA deteriorates significantly, and the peaks appear sparsely distributed. In fact, more peaks can be identified here at a magnified perspective. By including these peaks, we can state that the experimental quasi-BIC peaks are roughly uniformly spaced throughout this 250 GHz frequency range. This peak distribution corresponds to an average frequency spacing of 1.79 GHz between adjacent peaks.

Figure 6a shows that a single Si wafer can indeed produce a set of frequency comb-like resonances by utilizing quasi-BIC

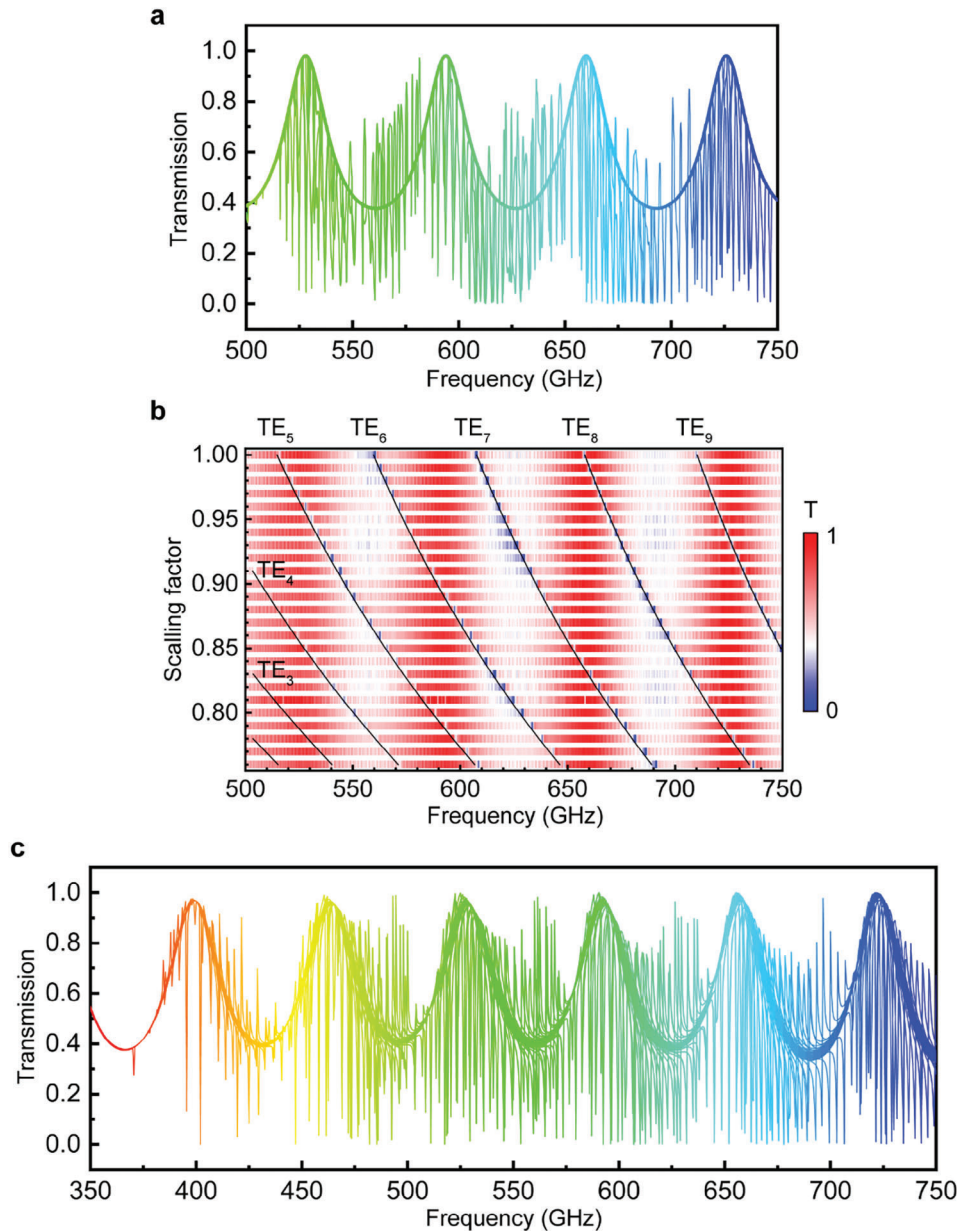


**Figure 6.** Transmission spectra of all the 25 metagrating pixels. a) Measured spectra, shown here by stitching all the peaks together. Several peaks at the low-frequency end are too weak to be discernible here as they approach the frequency edge of the measurement system, but they can still be identified in respective spectra at a magnified perspective. b) The whole set of measured spectral data, overlaid with frequency lines of relevant TE modes. c) Simulated spectra in a wider frequency range that spans over an octave. It is plotted following the style of panel (a). The frequency resolution is 0.1 GHz, the same as the experimental value.

resonances. The stitched spectrum also reveals a spectral background, which oscillates roughly between 0.4 and 1.0 for four cycles across the whole frequency range. This background oscillation originates from the Fabry–Pérot interference within the Si substrate. It may be undesirable for some applications and can be suppressed by adjusting the substrate thickness and the scaling factor  $S$ .

Different from Figure 6a, b shows all the experimental data, and specifies the corresponding TE modes for all the resonances. In the measured frequency range, each metagrating has five to

seven quasi-BIC peaks, thanks to the high-order BIC resonances. The order of the TE modes increases with frequency in each metagrating. For each order, it increases in frequency as the scaling factor  $S$  decreases. As discussed previously, the existence of multiple resonances in a single metagrating, together with the dependence of the resonance frequencies on  $S$ , facilitates the frequency comb-like peak distribution. By comparing Figure 6a against Figure 6b, we note that, other than the three  $TE_2$  peaks at the bottom-left corner of Figure 6b, all the quasi-BIC peaks predicted by the simulation are detected in the experiment.

Figure 6c shows all the simulated peaks, in order to compare with the experimental results of Figure 6a,b. A total of 241 peaks are obtained in the frequency range from 350 to 750 GHz. Among these 241 peaks, only two peaks are below 375 GHz, which are the TE<sub>0</sub> mode in the  $S = 1.00$  pixel (at 370.6 GHz) and that in the  $S = 0.99$  pixel (at 374.2 GHz). In the frequency octave from 375 to 750 GHz, except at the low-frequency end, the peak distribution is roughly uniform. A full list of the peak frequencies can be found in Table S1 (Supporting Information). For all the 140 peaks that both the experimental and the simulated frequency values are available, the maximal value of  $(f_m - f_s)/f_s$  is 0.36%, and the average of the absolute value  $|f_m - f_s|/f_s$  is 0.14%. Both values are very small, confirming the good matching between the simulated and the experimental results. It is worth noting that, to allow for a straightforward comparison with the experimental results, the simulated spectra of Figure 6c have a frequency resolution of 0.1 GHz, the same as the experiment. The resonances appear more uniform in peak intensity and frequency distribution, once a finer resolution is used in simulation (see Figure S1, Supporting Information, for the full set of spectra simulated at a frequency resolution of 0.01 GHz).

To highlight the significance of this work, we compare our results with several recent works that use multiplexing technologies to create multiple THz resonances in a single device (Table 1). As far as we know, our work is the only one that contains experimental verification. The table shows that our device has the highest peak numbers (241 in simulation, out of which 140 are detected) and a high peak density (close to refs. [35,37] and much higher than refs. [32,33]). It also covers a frequency octave, which has only been achieved previously in ref. [33].

### 3. Conclusion

To conclude, we have demonstrated a series of many, sharp, nearly uniformly spaced, quasi-BIC peaks on a single 6-inch Si wafer in the THz regime. The Si wafer is pixelated with 25 different metagratings, each metagrating supports multiple high-order quasi-BIC resonances, and a geometric scaling is applied across the metagrating array. By using these methods, a total of 241 sharp peaks are created in a frequency range from 350 to 750 GHz based on numerical simulation. Among these peaks, 140 are successfully confirmed experimentally, in the detection frequency range from 500 to 750 GHz. The experimental frequencies match well with the simulated results, and the relative frequency difference is only 0.14% on average. This work represents the first experimental demonstration of a series of frequency comb-like, quasi-BIC THz peaks on a single device, and opens a new route for molecule sensing in the THz regime. It could be particularly useful for distinguishing substances with highly similar THz fingerprints (e.g., table sugar and some plastic explosives), a capability that is greatly desired for THz sensing.

### 4. Experimental Section

**Microfabrication Procedure:** The wafer was ultrasonically cleaned in acetone and isopropyl alcohol (5 min each). It was then placed in gaseous hexamethyldisilazane (HMDS) for 10 min to prepare the surface for pho-

toresist coating. After that, photoresist (AZ Electronic Materials P4620) was spin coated on top of the wafer, before soft baking (at 100 °C for 120 s) on a hot plate. Photolithography was then conducted to pattern the metagratings (SUSS MicroTec MA8 mask aligner). After the pattern was developed, reactive ion etching (STS MCU21) was used to transfer the pattern from the photoresist onto the Si wafer (at an etching speed of  $\approx 5 \mu\text{m min}^{-1}$  for a total depth of 50  $\mu\text{m}$ ). The wafer was then cleaned by using acetone to remove the residual photoresist.

**Spectrum Measurement:** The measurement system consisted of several major components, including a vector network analyzer (Ceyear 3672), a THz transmitter module (Ceyear 3643U), two sets of lens adjustment modules, a sample positioning module, and a THz receiver module (Ceyear 3643U). The sample positioning module consisted of a rotation stage (Thorlabs RP01), two dovetail-bearing linear stages (Zolix DSM100S-65140L), and a high-load lab jack (Zolix MJ60). These components were used collectively for translational and rotational adjustment, a process assisted by the use of auxiliary components such as a visible laser. Two sets of TPX lenses (Tydex LPX-TPX-D38.1-F50) were used to collimate and focus the THz waves. The lenses were placed on bearing linear stages (Zolix TSMW13-XYZ-1AL) and rotation stages (Thorlabs RP01), for translational and rotational adjustment.

### Supporting Information

Supporting Information is available from the Wiley Online Library or from the author.

### Acknowledgements

This research was supported by the National Natural Science Foundation of China (grant no. 61927804). The authors acknowledge the “Explorer 100” cluster system of Tsinghua University for technical support.

### Conflict of Interest

The authors declare no conflict of interest.

### Data Availability Statement

The data that support the findings of this study are available from the corresponding author upon reasonable request.

### Keywords

bound states in the continuum, high-quality resonance, metagrating, quasi-bound states in the continuum, terahertz

Received: August 15, 2023

Revised: October 30, 2023

Published online:

- [1] M. Polese, J. M. Jornet, T. Melodia, M. Zorzi, *IEEE Commun. Mag.* **2020**, *58*, 48.
- [2] A. I. Nikitkina, P. Y. Bikmulina, E. R. Gafarova, N. V. Kosheleva, Y. M. Efmov, E. A. Bezrukov, D. V. Butnaru, I. N. Dolganova, N. V. Chernomyrdin, O. P. Cherkasova, A. A. Gavdush, P. S. Timashev, *J. Biomed. Opt.* **2021**, *26*, 043005.
- [3] W. Xu, Y. Huang, R. Zhou, Q. Wang, J. Yin, J. Kono, J. Ping, L. Xie, Y. Ying, *ACS Appl. Mater. Interfaces* **2020**, *12*, 44281.



- [4] Z. Yan, W. Shi, *J. Opt. Soc. Am. B* **2022**, *39*, A9.
- [5] M. C. Kemp, *IEEE Trans. Terahertz Sci. Technol.* **2011**, *1*, 282.
- [6] Y. Yang, I. I. Kravchenko, D. P. Briggs, J. Valentine, *Nat. Commun.* **2014**, *5*, 5753.
- [7] C. Jung, G. Kim, M. Jeong, J. Jang, Z. Dong, T. Badloe, J. K. W. Yang, *J. Rho, Chem. Rev.* **2021**, *121*, 13013.
- [8] J. Liu, X. Fang, F. He, S. Yin, W. Lyu, H. Geng, X. Deng, X. Zheng, *Opt. Express* **2021**, *29*, 21749.
- [9] W. Lyu, J. Liu, S. Yin, X. Deng, X. Fang, H. Geng, X. Zheng, *Opt. Express* **2022**, *30*, 12080.
- [10] L. L. Hale, H. Jung, S. D. Gennaro, J. Briscoe, C. T. Harris, T. S. Luk, S. J. Addamane, J. L. Reno, I. Brener, O. Mitrofanov, *ACS Photonics* **2022**, *9*, 1136.
- [11] Y. Huang, K. Kaj, C. Chen, Z. Yang, S. R. Ul Haque, Y. Zhang, X. Zhao, R. D. Averitt, X. Zhang, *ACS Photonics* **2022**, *9*, 1150.
- [12] H. Yang, P. He, K. Ou, Y. Hu, Y. Jiang, X. Ou, H. Jia, Z. Xie, X. Yuan, H. Duan, *Light: Sci. Appl.* **2023**, *12*, 79.
- [13] S. Shen, X. Liu, Y. Shen, J. Qu, E. Pickwell-Macpherson, X. Wei, Y. Sun, *Adv. Opt. Mater.* **2022**, *10*, 2101008.
- [14] C. Zhang, T. Xue, J. Zhang, L. Liu, J. Xie, G. Wang, J. Yao, W. Zhu, X. Ye, *Nanophotonics* **2022**, *11*, 101.
- [15] S. Lee, W. T. Kim, J.-H. Kang, B. J. Kang, F. Rotermund, Q.-H. Park, *ACS Appl. Mater. Interfaces* **2019**, *11*, 7655.
- [16] J. Li, Y. Zhang, J. Li, X. Yan, L. Liang, Z. Zhang, J. Huang, J. Li, Y. Yang, J. Yao, *Nanoscale* **2019**, *11*, 5746.
- [17] X. Chen, Z. Tian, Y. Lu, Y. Xu, X. Zhang, C. Ouyang, J. Gu, J. Han, W. Zhang, *Adv. Opt. Mater.* **2020**, *8*, 1900660.
- [18] X. Fu, F. Yang, C. Liu, X. Wu, T. J. Cui, *Adv. Opt. Mater.* **2020**, *8*, 1900628.
- [19] M. S. Islam, J. Sultana, M. Biabanifard, Z. Vafapour, M. J. Nine, A. Dinovtser, C. M. B. Cordeiro, B. W.-H. Ng, D. Abbott, *Carbon* **2020**, *158*, 559.
- [20] C. W. Hsu, B. Zhen, A. D. Stone, J. D. Joannopoulos, M. Soljacic, *Nat. Rev. Mater.* **2016**, *1*, 16048.
- [21] S. I. Azzam, A. V. Kildishev, *Adv. Opt. Mater.* **2021**, *9*, 2001469.
- [22] Z. Liu, Y. Xu, Y. Lin, J. Xiang, T. Feng, Q. Cao, J. Li, S. Lan, J. Liu, *Phys. Rev. Lett.* **2019**, *123*, 253901.
- [23] Y. Wang, Z. Han, Y. Du, J. Qin, *Nanophotonics* **2021**, *10*, 1295.
- [24] S. Yang, C. C. A. Hong, Y. X. Jiang, J. C. Ndukaife, *ACS Photonics* **2021**, *8*, 1961.
- [25] J. Li, J. Li, C. Zheng, Z. Yue, S. Wang, M. Li, H. Zhao, Y. Zhang, J. Yao, *Carbon* **2021**, *182*, 506.
- [26] N. Levanon, S. R. K. C. Indukuri, C. Frydendahl, J. Bar-David, Z. Han, N. Mazurski, U. Levy, *ACS Photonics* **2022**, *9*, 3642.
- [27] H. Zhang, W. Zhang, S. Chen, P. Duan, J. Li, L. Shi, J. Zi, X. Zhang, *Adv. Opt. Mater.* **2023**, *11*, 2203118.
- [28] A. Tittl, A. Leitis, M. Liu, F. Yesilkoy, D.-Y. Choi, D. N. Neshev, Y. S. Kivshar, H. Altug, *Science* **2018**, *360*, 1105.
- [29] J. Zhu, S. Jiang, Y. Xie, F. Li, L. Du, K. Meng, L. Zhu, J. Zhou, *Opt. Lett.* **2020**, *45*, 2335.
- [30] Y. Xie, X. Liu, F. Li, J. Zhu, N. Feng, *Nanophotonics* **2020**, *9*, 2927.
- [31] S. Ding, J.-Y. Ou, L. Du, L. Zhu, S. A. Khan, H. Chen, J. Zhu, *Carbon* **2021**, *179*, 666.
- [32] X.-J. Li, C. Ma, D.-X. Yan, S.-H. Guo, L. Zhang, J. Yang, Y. Zhao, W.-D. Zhou, *Opt. Lett.* **2022**, *47*, 2446.
- [33] L. Sun, L. Xu, J. Wang, Y. Jiao, Z. Ma, Z. Ma, C. Chang, X. Yang, R. Wang, *Nanoscale* **2022**, *14*, 9681.
- [34] D. Yan, Q. Feng, J. Yang, X. Li, L. Zhang, Y. Zhao, J. Li, *Phys. Chem. Phys.* **2022**, *25*, 612.
- [35] S. Liu, W. Chen, Y. Ma, Y. Xie, J. Zhou, L. Zhu, Y. Xu, J. Zhu, *Photonics Res.* **2022**, *10*, 2836.
- [36] Y. Xie, Y. Ma, X. Liu, S. A. Khan, W. Chen, L. Zhu, J. Zhu, Q. H. Liu, *IEEE J. Sel. Top. Quantum Electron.* **2023**, *29*, 1.
- [37] X. Zhang, J. Liu, J. Qin, *Nanoscale Adv.* **2023**, *5*, 2210.
- [38] Y. K. Srivastava, R. T. Ako, M. Gupta, M. Bhaskaran, S. Sriram, R. Singh, *Appl. Phys. Lett.* **2019**, *115*, 151105.
- [39] L. Hu, B. Wang, Y. Guo, S. Du, J. Chen, J. Li, C. Gu, L. Wang, *Adv. Opt. Mater.* **2022**, *10*, 2200193.
- [40] W. Shi, J. Gu, X. Zhang, Q. Xu, J. Han, Q. Yang, L. Cong, W. Zhang, *Photonics Res.* **2022**, *10*, 810.
- [41] F. Yang, J. Li, L. Wu, C. Zheng, Z. Yue, H. Li, C. Song, X. Ding, Y. Zhang, J. Yao, *Adv. Opt. Mater.* **2023**, *11*, 2300909.
- [42] A. Yariv, P. Yeh, *Optical Waves in Crystals: Propagation and Control of Laser Radiation*, Wiley, Hoboken, NJ, **1984**.
- [43] J. Dai, J. Zhang, W. Zhang, D. Grischkowsky, *J. Opt. Soc. Am. B* **2004**, *21*, 1379.
- [44] S. Han, L. Cong, Y. K. Srivastava, B. Qiang, M. V. Rybin, A. Kumar, R. Jain, W. X. Lim, V. G. Achanta, S. S. Prabhu, Q. J. Wang, Y. S. Kivshar, R. Singh, *Adv. Mater.* **2019**, *31*, 1901921.
- [45] H.-H. Hsiao, Y.-C. Hsu, A.-Y. Liu, J.-C. Hsieh, Y.-H. Lin, *Adv. Opt. Mater.* **2022**, *10*, 2200812.
- [46] K. Koshelev, S. Lepeshov, M. Liu, A. Bogdanov, Y. Kivshar, *Phys. Rev. Lett.* **2018**, *121*, 193903.